



Optimizing Brownian escape rates by potential shaping

Marie Chupeau^{a,b,1}, Jannes Gladrow^{c,1}, Alexei Chepelianskii^d, Ulrich F. Keyser^c, and Emmanuel Trizac^{a,2}

^aLaboratoire de Physique Théorique et Modèles Statistiques, CNRS, Université Paris-Sud, Université Paris-Saclay, 91405 Orsay, France; ^bMagic LEMP, 91400 Orsay, France; ^cCavendish Laboratory, University of Cambridge, Cambridge CB3 0HE, United Kingdom; and ^dLaboratoire de Physique des Solides, CNRS, Université Paris-Sud, Université Paris-Saclay, 91405 Orsay, France

Edited by Robert H. Austin, Princeton University, Princeton, NJ, and approved November 15, 2019 (received for review June 24, 2019)

Brownian escape is key to a wealth of physico-chemical processes, including polymer folding and information storage. The frequency of thermally activated energy barrier crossings is assumed to generally decrease exponentially with increasing barrier height. Here, we show experimentally that higher, fine-tuned barrier profiles result in significantly enhanced escape rates, in breach of the intuition relying on the above scaling law, and address in theory the corresponding conditions for maximum speed-up. Importantly, our barriers end on the same energy on which they start. For overdamped dynamics, the achievable boost of escape rates is, in principle, unbounded so that the barrier optimization has to be regularized. We derive optimal profiles under 2 different regularizations and uncover the efficiency of N-shaped barriers. We then demonstrate the viability of such a potential in automated microfluidic Brownian dynamics experiments using holographic optical tweezers and achieve a doubling of escape rates compared to unhindered Brownian motion. Finally, we show that this escape rate boost extends into the low-friction inertial regime.

Kramers problem | diffusion | variational optimization | holographic tweezers

Arrhenius law, a key principle of reaction kinetics, posits that chemical reactions become exponentially slower, the higher the activation energy barrier that reactants have to overcome[†]. In 1940, Kramers published a comprehensive theory for Arrhenius' scaling, introducing a framework for thermally activated transitions in an energy landscape. Importantly, in his theory, the system is coupled to the environment through friction and thermal noise. Further research has since revealed that swift thermal escapes from local potential energy minima require an intermediate friction magnitude such that motion is neither sluggish nor deterministic (2–6). However, influences of barrier shapes on escape rates and conditions of optimality thereof have been hitherto overlooked in the literature. In this paper, we theoretically optimize static barrier profiles, calculate the corresponding speed limit of escape, and demonstrate experimentally that higher, optimized barriers paradoxically result in increased escape rates, in contrast to intuition based on Kramers law. Since the maximum achievable escape rate is infinite, the barrier optimization has to be constricted, e.g., by placing an upper bound on the barrier height or curvature. In addition, we demonstrate experimentally a doubling of escape rates compared to unhindered Brownian motion, which proves that our predicted barrier profiles can indeed be realized. Furthermore, we show that the rate boost applies over a range of friction values, extending from the overdamped into the inertial regime. Our results indicate that fine-tuned free-energy landscapes of higher amplitude may increase reaction rates. In the context of protein folding, a carefully rate-optimized free-energy landscape may thus well exhibit a larger number of intermediate states despite additional necessary escapes (7).

We believe that this paper will invigorate a search for Brownian optimality and inform the design of systems where thermal excitation plays a role, such as adatom diffusion (8), chemical dynamics (9), polymer folding (10), and magnetic infor-

mation storage where thermal fluctuations limit capacity (11, 12). The question of optimizing the potential profile becomes timely in view of the spectacular experimental progress made in controlling confining features for colloidal objects (13–15).

The rate of progress of Brownian or other stochastic processes is not easily quantifiable. One way to measure the “speed” of Brownian motion is the mean first-passage time (FPT) to a given distance (16, 17). In Kramers' escape problem, the reciprocal of the escape rate corresponds to the time of first passage to leave the initial state. A lower bound for the achievable FPT, e.g., of the reaction coordinate of a folding molecule, therefore corresponds to a speed limit of the ensemble reaction rate (18).

Introductory Example

To illustrate the speed-up of the mean FPT across potential barriers, we consider the triangular barrier profile in Fig. 1A. This profile has been shown to decrease first-passage times of overdamped Brownian motion, relative to a linear potential (19). Importantly, this profile-induced speed-up does not require any expense in energy[‡]: The effect also appears in energy-neutral potential profiles, constructed in such a way that initial and final

Significance

Diffusion is of fundamental relevance in physics, chemistry, and biology, to explain the transport of macromolecules in a solvent, under the action of external forces. Diffusion is fueled by temperature, resulting in thermal fluctuations. Macromolecules trapped in a potential energy well can then escape, harnessing favorable fluctuations. Such events are a priori rare nevertheless, and the so-called Arrhenius relation describes the corresponding exponential decrease of escape rates with increasing barrier heights. It therefore comes as a surprise that some potential wells, with high barriers, may help the macromolecule escape. We report experimental proof of this counterintuitive boosting effect. Optimizing theoretically the potential profile that provides maximum boost, we translate our predictions into results in automated microfluidic experiments.

Author contributions: M.C., J.G., A.C., U.F.K., and E.T. designed research, performed research, and wrote the paper.

The authors declare no competing interest.

This article is a PNAS Direct Submission.

Published under the PNAS license.

See online for related content such as Commentaries.

¹M.C. and J.G. contributed equally to this work.

²To whom correspondence may be addressed. Email: trizac@lptms.u-psud.fr.

This article contains supporting information online at <https://www.pnas.org/lookup/suppl/doi:10.1073/pnas.1910677116/-DCSupplemental>.

First published December 16, 2019.

[†]Arrhenius himself attributed this law to van't Hoff (1, 2).

[‡]If “position” x refers to a reaction coordinate subsuming a complex landscape, the free energy, rather than the energy, should be considered. This distinction is immaterial for our one-dimensional discussion.

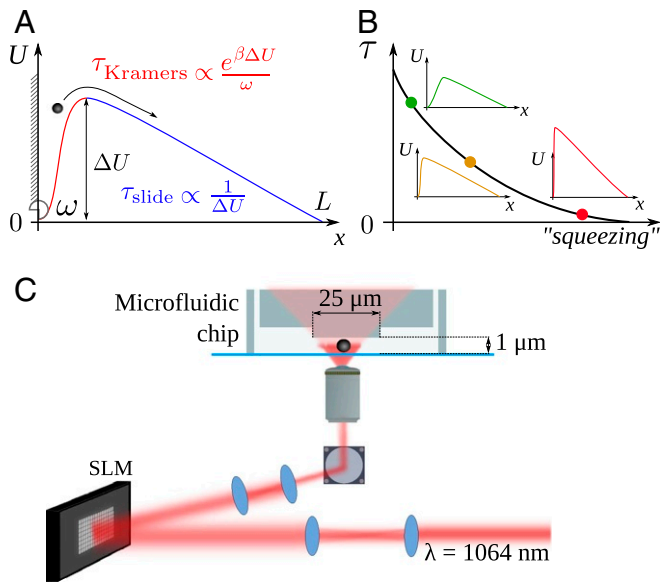


Fig. 1. (A) Simple potential profile, characterized by its height ΔU and the curvature of the associated potential well ω . The 2 key timescales in the overdamped exit process are the Kramers' escape time[¶] and the slide time. For such a profile and provided that ΔU is large enough, the exit time simplifies into $\tau \simeq \tau_{\text{Kramers}} + \tau_{\text{slide}}$. Increasing ΔU (to decrease τ_{slide}) and ω in the appropriate fashion leads to enhanced "squeezing" of the well and to a decrease of τ (shown in B). In doing so, ΔU diverges while τ can be made as small as desired. Thus, imposing the constraint $|U(x)| < U_{\text{max}}$ or discretizing space will lead to a nonzero optimal time τ (cases/constraints A and B in main text). This regularizes the vanishing of τ , that is, a specificity of the overdamped description. The underdamped regime does not require regularization. We generally understand "underdamped" as meaning "nonoverdamped." The overdamped regime is such that there are infinitely many potential shapes that lead to the optimal escape time $\tau = 0$. A constrained (regularized) problem is such that $\tau \neq 0$. (C) Sketch of the holographic optical tweezers setup used to measure escape times over optimized barriers that are shaped by creating intensity and phase profiles inspired by predicted optimal potential profiles.

energy levels coincide[§]. The particle in Fig. 1A is initialized at $x = 0$ in the narrow well (red region), and our interest goes to the first passage at $x = L$. The movements are bounded by a reflecting barrier at $x = 0$ and an absorbing boundary at $x = L$. The mean escape time from the narrow well is given by Kramers' result $\tau_{\text{Kramers}} \propto e^{\beta\Delta U}/\omega$ with $\beta = 1/(kT)$ denoting the inverse temperature times the Boltzmann constant $k^{\#}$. Once out of the well, the particle slides toward the exit within an average slide time $\tau_{\text{slide}} \propto 1/\Delta U$ as follows from gradient descent. In the limit of high barriers, the overall mean exit time τ reads as the sum of τ_{Kramers} and τ_{slide} (19); it can therefore be made arbitrarily small by simultaneously increasing the steepness and height of the initial well (Fig. 1B). Crucially, a sufficiently high and steep barrier yields a mean exit time shorter than the corresponding free diffusion time $\tau_{\text{free}} = L^2/(2D)$, where D is the diffusion coefficient (24). Moreover, there is no lower bound (other than zero) for the exit time: Further "squeezing" will further decrease τ (Fig. 1B). The exit time approaches zero for appropriately chosen diverging

curvature and barrier height. Fig. 1C presents the experimental setup used in this work to test the predictions.

Barrier Profile Optimization

In the following, all relevant quantities, the mean exit time, the potential, and the abscissa are conveniently rescaled: $\tilde{\tau} = D\tau/L^2$, $\tilde{U} = \beta U$, $\tilde{x} = x/L$, where $D = 1/(\beta m \gamma)$ defines the temperature T that drives the Brownian process, m the particle mass, and γ the friction coefficient. Tildes denote dimensionless variables, but are dropped hereafter, unless otherwise stated. The mean exit time is given by (23, 25)

$$\tau = \int_0^1 dx e^{-U(x)} \int_x^1 dy e^{U(y)}, \quad [1]$$

which is invariant under the transformation $U(x)$ to $-U(1-x)$ (SI Appendix). A joint use of this invariance and Cauchy-Schwarz inequality shows that the optimal potential is necessarily antisymmetric with respect to $x = 1/2$ (such that $U(x) = -U(1-x)$), provided that the constraints on the potential are compatible with antisymmetry transformation (see SI Appendix for details). The 2 distinct constraints we discuss in the following, (constraint A) bounds on U and (constraint B) regular space discretization, are both compatible with antisymmetry.

Constraint A—Symmetrically Bound Potential. Imposing bounds on the potential offers the most straightforward regularization to discuss optimality. For the sake of simplicity, we restrict ourselves to constant bounds $U_{\text{min}} \leq U(x) \leq U_{\text{max}}$ and refer to this constraint as A.

By minimizing τ in Eq. 1 with respect to U , we show in SI Appendix that the optimal potential A obeys

$$e^{U(y)} \int_0^y dx e^{-U(x)} = e^{-U(y)} \int_y^1 dx e^{U(x)}. \quad [2]$$

It follows that it has the generic shape sketched in Fig. 2A, which consists of 2 plateaus on the upper and lower bounds, connected by a decreasing linear part. The positions x^* and y^* of the intersection between the 2 plateaus and the linear part can also be calculated, as well as the associated optimal mean exit time

$$\tau_{\text{opt}}^A = x^* = 1 - y^* = \frac{1}{2 + U_{\text{max}} - U_{\text{min}}}. \quad [3]$$

For symmetric bounds $U_{\text{min}} = -U_{\text{max}}$, the optimal potential is antisymmetric, as expected. For general bounds, the optimal mean exit time depends only on the potential difference $\Delta U = U_{\text{max}} - U_{\text{min}}$ and is always smaller than the free diffusion time $\tau_{\text{free}} = 1/2$. Moreover, when the potential difference is much larger than one, we obtain

$$\tau_{\text{opt}}^A \Delta U \simeq 1. \quad [4]$$

This expression is reminiscent of Heisenberg's time-energy uncertainty principle, even though the problem is, of course, purely classical. The larger the amplitude of the potential is, the shorter the mean exit time. Eq. 4 also implies that the scaling of the mean exit time reduces, at leading order, to the slide time-scaling $1/\Delta U^{\#}$. This result is in accord with the fact that the plateaus disappear at large ΔU . This phenomenology also applies in higher-dimensional systems, as shown in SI Appendix.

[§]In nonneutral (tilted) landscapes where net work is performed, interesting effects have been reported. For instance, diffusion coefficients in tilted periodic potentials can vastly exceed their free diffusion value, which leads to a "giant acceleration" of diffusion (20–22).

[¶]Assuming the bottom of the well together with the top of the barrier to be parabolic, with respective curvatures $m\omega^2$ and $-m\omega_{\text{top}}^2$ where m is the particle mass, Kramers' escape time reads (23) $\tau_{\text{Kramers}} \propto \omega^{-1}\omega_{\text{top}}^{-1} \exp[\Delta U/(kT)]$, $\Delta U > 0$.

[#]Going back to dimensioned quantity, this corresponds to a speed $\tau/L \propto U/(m\gamma L)$, where temperature drops out. This is nothing but the sliding time in the constant force field U/L , with a mobility $1/(m\gamma)$. The initial escape from $x = 0$ to the plateau at $x = 0^+$ (and likewise the jump from $x = L^-$ to $x = L$) occurs in a vanishing time, within the present overdamped formulation.

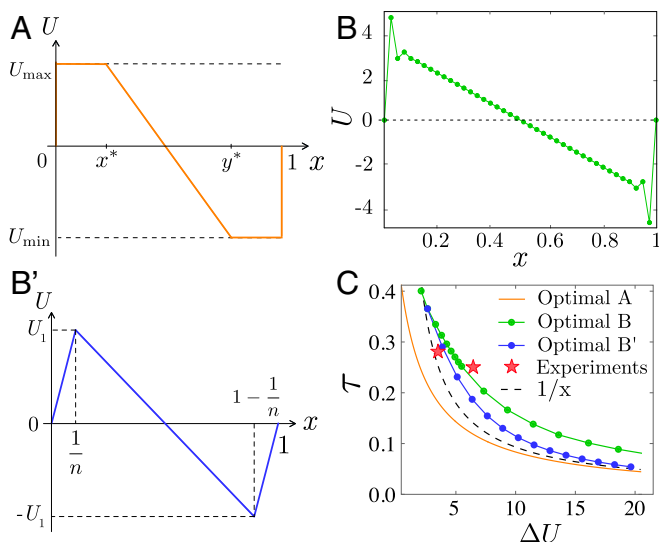


Fig. 2. (A) Optimal potential profile A with bounds U_{\min} and U_{\max} . (B) Optimal potential B for a 40-support potential. The potential is not bounded anymore. (B') N-shaped approximation of the discretized case, with only one variable parameter U_1 (optimal potential B'). (C) Mean exit time as a function of the potential barrier, for the optimal potentials A, B, and B'. The color code is consistent in A–C. The dashed line represents the asymptotics $1/\Delta U$, valid for optimal potentials A and B'. Because of its overshoots, the optimal potential B has different asymptotics. The red stars correspond to the experimental data (Fig. 3).

Despite its convenience, constraint A possesses one drawback: the nonphysical discontinuity of the corresponding optimal potential A^{||}.

Constraint B—Piecewise-Linear Potential. We therefore turn to constraint B, for which the potential is a piecewise linear function, defined by n nodes (x_i, U_i) where we require the x_i to be regularly spaced in $[0, 1]$. We refer to such a profile as an n -support function. As before, the potential is chosen to be energy neutral; that is, $U_0 = U_{n+1} = 0$. Contrarily to constraint A, constraint B does not impose any restriction on the value of U_i (U is a priori not bounded). As shown in *Introductory Example*, large potential barriers can be efficient only when the width of the associated well vanishes. Here, the well width is bounded from below by $1/n$, the spatial discretization step, so that bounding the potential becomes unnecessary. To compute the associated optimal potential profile B, we carry out simulated annealing. Fig. 2B provides an example of optimal potential B for a 40-support one. It is antisymmetric as expected and reminiscent of an “N shape” with an overshoot and an undershoot on both sides of the intermediary slide. The overshoot prevents the particle from recrossing the barrier and falling back into the initial well. Its amplitude is determined by a trade-off between a quick escape from the initial well, a low recrossing probability, and a short slide time. A simple approximation of this optimal potential profile is given by the N-shaped function (denoted B'), only parameterized by the potential barrier height U_1 , as shown in Fig. 2B'. A minimization of Eq. 1 for this potential profile yields a $\ln n$ scaling of the parameter U_1 , and the corresponding mean exit time

$$\tau_n^{B'} = \frac{1}{2 \ln n} + o\left(\frac{1}{\ln n}\right). \quad [5]$$

^{||} $U(0) = U(1) = 0$ by construction, while $U(0^+) = U_{\max}$ and $U(1^-) = U_{\min}$.

Although optimal potential B' cannot exhibit an overshoot, it captures the correct scaling of the mean exit time which is, as for constraint A, given by the sliding time. In particular, to leading order in n , the mean exit time and the total potential difference $\Delta U = 2U_1$ still verify $\tau_n^{B'} \Delta U \simeq 1$. The overshoot structure of optimal potential B can be satisfactorily described by a 2-parameter potential ansatz. Once optimized, it turns out that this overshoot structure modifies the subleading order of Eq. 5, yielding only a slightly smaller mean exit time than with optimal potential B'. It is interesting here to note that a profile, reminiscent of our N shape, was also reported in a discrete model of molecular transport through nanopores (26).

To compare the efficiency of the differently constrained potentials, we use the total potential amplitude $\Delta U = \max_x |U(x)|$ as an index. This leads to Fig. 2C. According to this criterion, the optimal potential A (Fig. 2A) is of course the most efficient, but displays discontinuities. By contrast, the optimal potential B (Fig. 2B) is continuous but only poorly efficient, since it requires a large amplitude due to the over- and undershoots, which nevertheless do not significantly reduce the mean exit time. A good compromise is given by the N-shaped reasonably efficient optimal potential B' (Fig. 2B'), which we realized experimentally as we describe below.

Experimental Design and Results

To test whether experimental potentials can be tailored to deliver the predicted speed-ups, we leveraged the ability of a holographic optical tweezer (HOT) to create almost arbitrary intensity and phase patterns in the focal plane of a microscope (27, 28). In addition, we used a microfluidic device to confine movements of colloidal particles, to a quasi-one-dimensional line, eliminating entropic forces and variations in hydrodynamic friction (29, 30). The motion of colloidal particles is well within the overdamped regime, such that our theory applies. All experiments were carried out by an automated “drag-and-drop” routine based on a real-time recognition system, which is able to locate colloidal particles and displace them using individually addressable dynamic holographic traps (31).

As a first step, we measured first-passage times τ_0 of a colloid released in the center of a channel, shown in Fig. 3A, without the influence of laser forces (Fig. 3B). As the data in Fig. 3C show, these times adhere closely to theory and scale quadratically with distance. From this dataset, we infer a diffusion coefficient of $D = 0.23 \mu\text{m}^2/\text{s}$.

The holographic parameters necessary to form the right balance of intensity-gradient and phase-gradient forces (32) were found by trial and error. Specifically, the N-shaped potential was created by a combination of a single point trap providing the initial potential well and 3 line traps with phase gradients and lengths as specified in *SI Appendix*.

The resulting potential landscape $U(x)$ was obtained by integrating forces $f(x)$, which we inferred along the channel from binned displacement statistics $\rho_x(\Delta x) \propto \exp\left[-\frac{(\Delta x - \Delta t f(x)/(m\gamma))^2}{4D\Delta t}\right]$. The friction coefficient γ was calculated from the measured diffusion coefficient using $m\gamma = k_B T/(D)$ (see *SI Appendix*, Eq. S1). Our passive potential inference works reliably for shallow potential wells $\Delta U < 5 k_B T$; inference of deeper minima would require intervention (33). As Fig. 3D shows, the potential largely adheres to the desired N shape, except for a few wiggles, which are due to optical aberrations and interference (*SI Appendix*).

The obtained mean first-passage time is plotted in Fig. 3E, as well as the free-diffusion fit. The profile speed-up introduced by the intermediary slide part of this potential is clearly visible. It results in a mean exit time of 336 ± 19 s, compared to the 684 s for free diffusion; hence we obtain a speed-up factor of 2. This experimental measurement is displayed in Fig. 2C with

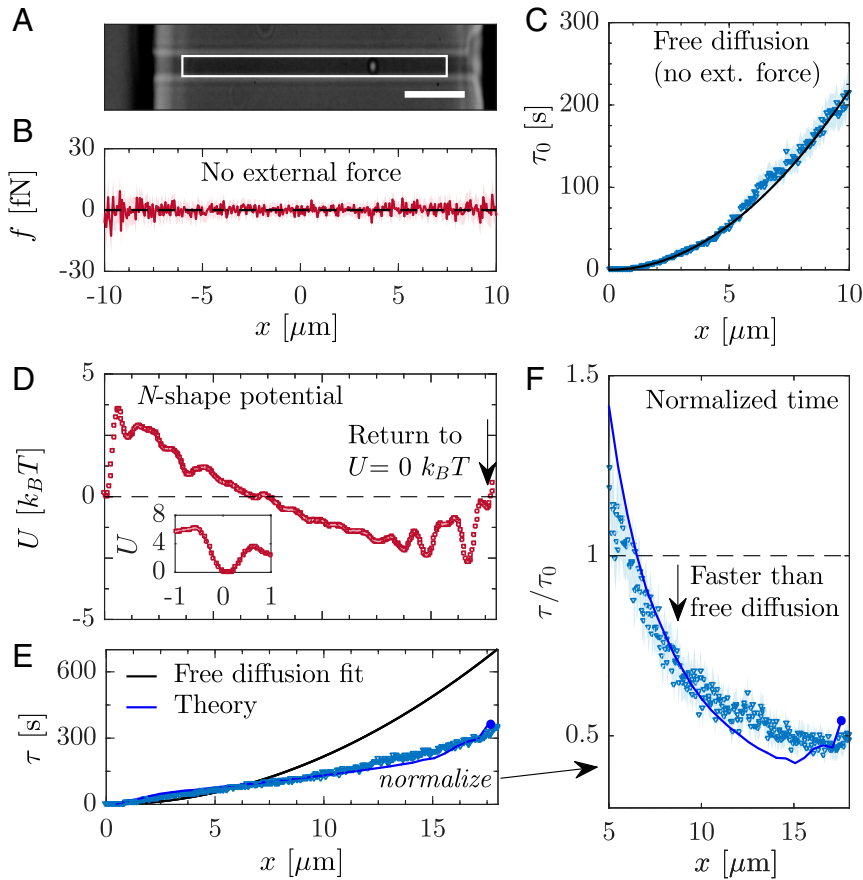


Fig. 3. (A) Picture of microfluidic channel used, containing a single particle. The region of interest used subsequently is shown with the frame. (B) Forces along the channel inferred for the zero-potential case. The error envelope is on the order of the marker size. We here plot the force rather than the potential to highlight the accuracy of our force estimator. (C) First-passage time measured symmetrically from the center of an interval in the absence of optical forces. (Scale bar, 5 μm .) (D) N-shaped potential created by the HOT, corresponding to the rightmost star in Fig. 2C (the other experiment is described in *SI Appendix*). Inset shows the asymmetric barrier used to approximate the initial reflecting boundary. (E) Measured first-passage times at position x for the same potential compared with the free-diffusion fit. (F) Measured first-passage time at position x , normalized by the corresponding free diffusion time $x^2/(2D)$.

a star. The experimental landscape has a lower efficiency than the targeted optimized N-shaped potential. This is caused by aberrations and interference between different holographic elements, but despite these imperfections, a significant speed-up is achieved.

The Underdamped Regime

Finally, energy profile optimization raises a conceptual problem. Provided that the constraint is loose enough (large ΔU or large n , for example), the optimal mean exit time becomes sufficiently low and may leave the range of validity of the overdamped regime (23). Therefore, we need to extend the discussion to the underdamped situation, where the state of the particle is characterized by both its position and its velocity (*SI Appendix*). Then, inertia matters, and the particle's velocity cannot instantaneously adjust to the force applied. This delay causes a nontrivial response to forcing. To proceed, we introduce some additional rescalings $\tilde{v} = v\sqrt{m/(kT)}$ and $\tilde{\gamma} = \gamma L\sqrt{m/kT}$, where tildes will again be implicit in the following. Although not consistent with the rescalings on position and velocity, we keep the same rescaling for time as in the overdamped case, for better comparison with this limit. Extracting the mean exit time from the statistical description of the underdamped problem is more involved than in the overdamped case, and no general analytical expression is known. Even the free diffusion case requires cumbersome

calculations (34, 35). However, a development in terms of harmonic oscillator eigenfunctions can be carried out (36). Keeping the first 2 orders, we find (*SI Appendix*)

$$\begin{aligned} \tau \simeq & \int_0^1 dx \int_x^1 dz e^{U(z)-U(x)} + \frac{1}{\gamma} \sqrt{\frac{\pi}{2}} \int_0^1 dx e^{-U(x)} \\ & + \frac{1}{\gamma^2} \left[-\frac{U'(1)}{2} \int_0^1 dx e^{-U(x)} \right. \\ & \left. + \int_0^1 dx \int_x^1 dz U'^2(z) e^{U(z)-U(x)} \right], \end{aligned} \quad [6]$$

here for an initially thermalized particle starting on the reflecting boundary. As expected, the zero-order term corresponds to the overdamped expression Eq. 1. Then, the first-order term in $1/\gamma$ penalizes negative parts of the potential and favors positive ones, resulting in an antisymmetry breaking of the optimal potential for finite friction. As for the second-order term, its first part favors negative increasing profiles near $x = 1$, whereas its second part, that is mainly significant around the maximum of the profile, favors height reduction of the first barrier as well as its bending.

To test this theoretical prediction and work out arbitrary damping, we implement a simulated annealing optimization coupled to a finite-element method (*SI Appendix*). To facilitate

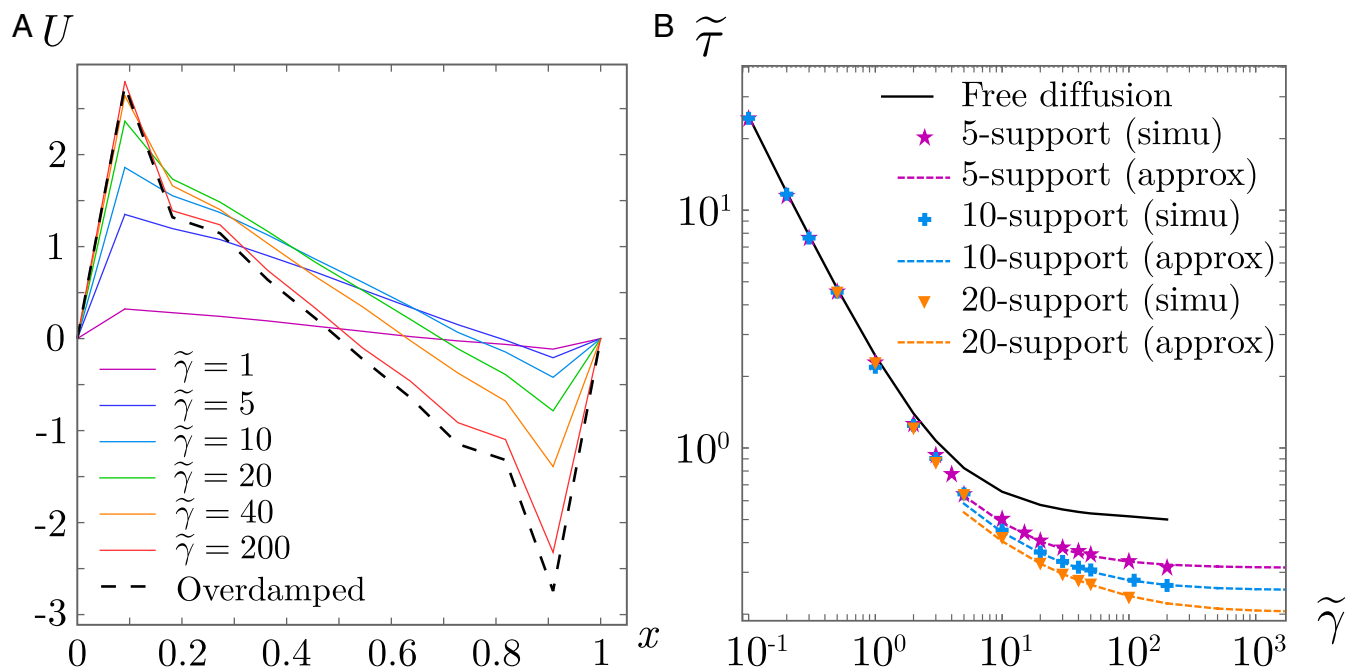


Fig. 4. (A) Optimal 10-support potential profiles for various frictions, compared to the overdamped limit. (B) Evolution of the optimal mean exit time with friction, for 5-, 10-, and 20-support potentials, obtained by finite-element annealing (*SI Appendix*). Dashed lines correspond to optimization carried out with Eq. 6.

comparison with the overdamped limit, we restrict the optimization to n -support functions. Fig. 4A shows how a decrease in friction impinges on the optimal potential profile. It confirms the expectation based on Eq. 6, such as the breakdown of antisymmetry, reduction of the amplitude of the optimal profile, and bending of the profile around its maximum with the disappearance of the overshoot. We compare the resulting optimized mean exit time with the free case in Fig. 4B. Interestingly, the profile speed-up does extend beyond the overdamped limit. However, its efficiency decreases when friction decreases. In very underdamped situations, despite the momentum gained in the intermediary slide part, the cost for well escape becomes prohibitive. Our results indicate that in the case of vanishing friction, the optimal shape will converge to a constant potential. The profile speed-up is therefore most relevant in the moderately damped to overdamped regimes.

Conclusion

We have studied profile speed-up of a Brownian particle by an energy-neutral potential barrier. We optimized this process under 2 complementary constraints, which either bound the potential directly or require regular spatial discretization. From the optimal potentials obtained, we constructed an efficient

experiment-friendly profile that we implemented using a combination of optical and microfluidics techniques. We were thereby able to accelerate the exit dynamics of a colloid in a narrow channel by a factor of 2. Moreover, the profile speed-up is not specific to overdamped systems and is observed, although with lower magnitude, at arbitrary damping. Altogether, the profile-induced speed-up then appears to be robust and relevant in a large range of friction values. Finally, although the emphasis was here in the one-dimensional setting, our results extend to higher dimensions, as discussed in *SI Appendix*. While a comprehensive analytical treatment of this problem beyond the overdamped limit remains a considerable theoretical challenge, our results anyway require a rethink of the seemingly settled problem of reaction rates and Brownian transport.

Materials are available on request.

ACKNOWLEDGMENTS. We thank O. Giraud, Y. Tourigny, and F. van Wijland for useful discussions and critical reading of the manuscript. We acknowledge funding from the Investissement d'Avenir LabEx PALM program (Grant ANR-10-LABX-0039-PALM). The research leading to these results has also received funding from the European Union's Horizon 2020 research and innovation program under Innovative Training Network Grant 674979-NANOTRANS. U.F.K. acknowledges funding from an European Research Council Consolidator Grant (DesignerPores 647144).

- S. Arrhenius, Über die reaktionsgeschwindigkeit bei der inversion von rohrzucker durch säuren. *Z. Phys. Chem.* **4**, 226 (1889).
- P. Hänggi, P. Talkner, M. Borkovec, Reaction-rate theory: Fifty years after Kramers. *Rev. Mod. Phys.* **62**, 251–341 (1990).
- H. A. Kramers, Brownian motion in a field of force and the diffusion model of chemical reactions. *Physica* **7**, 284–304 (1940).
- V. I. Mel'nikov, The Kramers problem: Fifty years of development. *Phys. Rep.* **209**, 1–71 (1991).
- N. Kiesel, E. Lutz, Levitated nanoparticles: Nanoparticles jumping high. *Nat. Nanotechnol.* **12**, 1119–1120 (2017).
- L. Rondin *et al.*, Direct measurement of Kramers turnover with a levitated nanoparticle. *Nat. Nanotechnol.* **12**, 1130–1133 (2017).
- C. Wagner, T. Kiefhaber, Intermediates can accelerate protein folding. *Proc. Natl. Acad. Sci. U.S.A.* **96**, 6716–6721 (1999).
- R. Guantes, J. L. Vega, S. Miret-Artés, E. Pollak, Kramers turnover theory for diffusion of Na atoms on a Cu(001) surface measured by He scattering. *J. Chem. Phys.* **119**, 2780 (2003).

- P. L. García-Müller, F. Borondo, R. Hernandez, R. M. Benito, Solvent-induced acceleration of the rate of activation of a molecular reaction. *Phys. Rev. Lett.* **101**, 178302 (2008).
- R. B. Best, G. Hummer, Diffusive model of protein folding dynamics with Kramers turnover in rate. *Phys. Rev. Lett.* **96**, 228104 (2006).
- W. T. Coffey, Y. P. Kalmykov, Thermal fluctuations of magnetic nanoparticles: Fifty years after Brown. *J. Appl. Phys.* **112**, 121301 (2012).
- G. M. Rotskoff, G. E. Crooks, E. Vanden-Eijnden, Geometric approach to optimal nonequilibrium control: Minimizing dissipation in nanomagnetic spin systems. *Phys. Rev. E* **95**, 012148 (2017).
- P. Miles, B. Richard, Tweezers with a twist. *Nat. Photonics* **5**, 343–348 (2011).
- I. A. Martinez, A. Petrosyan, D. Guéry-Odelin, E. Trizac, S. Ciliberto, Engineered swift equilibration of a Brownian particle. *Nat. Phys.* **12**, 843–846 (2016).
- S. Ciliberto, Experiments in stochastic thermodynamics: Short history and perspectives. *Phys. Rev. X* **7**, 021051 (2017).
- A. B. Kolomeisky, E. B. Stukalin, A. A. Popov, Understanding mechanochemical coupling in kinesins using first-passage-time processes. *Phys. Rev. E* **71**, 031902 (2005).

17. S. Redner, *A Guide to First Passage Processes* (Cambridge University Press, 2001).
18. J. Kubelka, J. Hofrichter, W. A. Eaton, The protein folding 'speed limit'. *Curr. Opin. Struct. Biol.* **14**, 76–88 (2004).
19. V. V. Palyulin, R. Metzler, How a finite potential barrier decreases the mean first-passage time. *J. Stat. Mech. Theory Exp.*, L03001 (2012).
20. P. Reimann *et al.*, Giant acceleration of free diffusion by use of tilted periodic potentials. *Phys. Rev. Lett.* **87**, 010602 (2001).
21. S. H. Lee, D. G. Grier, Giant colloidal diffusivity on corrugated optical vortices. *Phys. Rev. Lett.* **96**, 190601 (2006).
22. D. Kim, C. Bowman, J. T. Del Bonis-O'Donnell, A. Matzavinos, D. Stein, Giant acceleration of DNA diffusion in an array of entropic barriers. *Phys. Rev. Lett.* **118**, 048002 (2017).
23. J.-L. Barrat, J.-P. Hansen, *Basic Concepts for Simple and Complex Liquids* (Cambridge University Press, 2003).
24. C. Gardiner, *Stochastic Methods: A Handbook for the Natural and Social Sciences* (Springer-Verlag Berlin, Germany, 2009).
25. N. G. Van Kampen, *Stochastic Processes in Physics and Chemistry* (Elsevier, 1992), vol. 1.
26. A. B. Kolomeisky, U. Karthik, How interactions control molecular transport in channels. *J. Stat. Phys.* **142**, 1268–1276 (2011).
27. J. E. Curtis, B. A. Koss, D. G. Grier, Dynamic holographic optical tweezers. *Opt. Commun.* **217**, 169–175 (2012).
28. J. Gladrow, M. Ribezzi-Crivellari, F. Ritort, U. F. Keyser, Experimental evidence of symmetry breaking of transition-path times. *Nat. Commun.* **10**, 55 (2019).
29. R. Zwanzig, Diffusion past an entropy barrier. *J. Phys. Chem.* **96**, 3926–3930 (1992).
30. X. Yang *et al.*, Hydrodynamic and entropic effects on colloidal diffusion in corrugated channels. *Proc. Natl. Acad. Sci. U.S.A.* **114**, 9564–9569 (2017).
31. R. W. Bowman *et al.*, Red tweezers: Fast, customisable hologram generation for optical tweezers. *Comput. Phys. Commun.* **185**, 268–273 (2014).
32. Y. Roichman, B. Sun, Y. Roichman, J. Amato-Grill, D. G. Grier, Optical forces arising from phase gradients. *Phys. Rev. Lett.* **100**, 013602 (2008).
33. M. P. N. Juniper, R. Besseling, D. G. A. L. Aarts, R. P. A. Dullens, Acousto-optically generated potential energy landscapes: Potential mapping using colloids under flow. *Opt. Express* **20**, 28707 (2012).
34. P. S. Hagan, C. R. Doering, C. D. Levermore, The distribution of exit times for weakly colored noise. *J. Stat. Phys.* **54**, 1321–1352 (1989).
35. J. Masoliver, J. M. Porrà, Exact solution to the mean exit time problem for free inertial processes driven by Gaussian white noise. *Phys. Rev. Lett.* **75**, 189–192 (1995).
36. H. Risken, "Fokker-Planck equation" in *The Fokker-Planck Equation*, H. Haken, Ed. (Springer, 1996), pp. 63–95.